Finite Element Comparison of Homogenous Ridged and Non-Ridged X-Band Rectangular Waveguide Dispersion Characteristics

Samuel J. Wyss†
†School of Nuclear Engineering
Purdue University
West Lafayette, Indiana 47907
E-mail: wysss@purdue.edu

***Abstract*—Two dimensional Finite Element Analysis (FEA) is applied to assess dispersion characteristics of homogenous rectangular, circular and ridged rectangular X-Band waveguides. To model these systems *in silico*, the weak form of the wave equation is derived from Maxwell's Equations for both TE and TM modes. Perfect electrical conductors (PECs) are used as waveguide walls as to neglect the effect of wave leakage into the environment. The model is validated against the analytical dispersion curves for homogenous rectangular waveguides. Dispersion characteristics of circular waveguides are assessed. A comparison of dispersion characteristics for ridged and non-ridged rectangular waveguides is provided which is then used to assess real world applications of ridged waveguides.**

I. Introduction

Waveguides are used in a plethora of applications ranging from transmitting microwave fields to acting as passive, low-pass filters [1]. While any cross section of a single conductor waveguide can support TE and TM modes, rectangular and circular cross sections are commonly chosen due to their ease of construction and analytic propagation characteristics. However, a limitation of rectangular waveguides is the limited bandwidth of their dominant mode which is less than an octave [1]. By adding a single or double ridge to the mouth of a waveguide, the cutoff frequency of the dominant mode can be reduced thus allowing for increased signal bandwidth [1]. This increased bandwidth comes at the cost of reduced power capacity due to the reduction in breakdown potential between the ridges [1] making them less ideal for High Power Microwave (HPM) devices.

All wave phenomenon in an arbitrarily shaped, infinitely long waveguide at a given frequency are governed by the frequency domain Maxwell's Equations. Of these equations, Faraday's and Ampère's laws, can be manipulated to create Helmholtz wave equations which capture nearly all electromagnetic wave phenomenon to a high degree of accuracy [2]. The Finite Element Method (FEM) converges on the analytic solution of the wave equation by approximating a weak form of the Helmholtz equations over a finite set of elements within the simulation domain using weighted residuals. To convert the full wave equation to its weak form, the Galerkin method is employed for which the weighting functions are identical to continuous basis functions as is common in Computational Electromagnetics (CEM) Finite Element Analyis (FEA) [2]. In the case of an arbitrarily shaped, infinitely long waveguide, the full-field, frequency-domain solutions can be obtained by solving for the fields in a cross sectional slice of the waveguide. FEM operates on non-uniform, conformal meshes which allows for arbitrary waveguide cross sections to be modeled without stairstepping error unlike that of the structured meshes of Finite-Difference Time-Domain (FDTD). In addition to this, FEM allows for full three dimensional solutions of such a waveguide to be obtained by only solving for a representative two dimensional slice making FEM an ideal choice for analyzing homogenous waveguides.

The development and results of this work are laid out as follows. Section II contains derivations of the Galerkin weak forms of the Helmholtz wave equations for both the TE and TM modes as well as the formation of the FEM matrices via the assembly process. Section III contains a verification of the model with analytic data for a square waveguide, an analysis and discussion of propagation in circular waveguides, as well as a comparison of rectangular waveguides to their ridged counterparts. Finally, Section IV contains closing remarks regarding the analysis and potential future work.

II. Mathematical Model

To model these systems *in silico*, an appropriate mathematical model must first be derived from Maxwell's Equations. The development of said model model is arranged as follows. Section II-1 contains the derivation of the Helmholtz wave equations and corresponding boundary conditions from Maxwell's Equations. Section II-2 consists of the derivation of the Galerkin weak form of both Helmholtz wave equations. Section II-3 outlines the FEM assembly method using analytical forms of integrals derived in II-2.

1) Governing Equations: The frequency domain Maxwell's Equations in the absence of electric or fictitious magnetic currents are,

$$\nabla \times \mathbf{E} = -j\omega\mathbf{B}, \tag{1}$$

and

$$\nabla \times \mathbf{H} = -j\omega\mathbf{D} \tag{2}$$

where **E** is the electric field intensity, **B** is the magnetic flux density, **H** is the magnetic field intensity, and **D** is the electric flux density.

For a homogenous, infinite waveguide filled with a non-dispersive dielectric, **B** and **D** can be rewritten as

$$\mathbf{B} = \mu\mathbf{H}, \tag{3}$$

and

$$\mathbf{D} = \epsilon\mathbf{E}. \tag{4}$$

These constitutive relations can now be used to simplify (1-2) as in

$$\nabla \times \mathbf{E} = -j\omega\mu\mathbf{H}, \tag{5}$$

and

$$\nabla \times \mathbf{H} = -j\omega\epsilon\mathbf{E}. \tag{6}$$

In the case of the infinite waveguide, the TM and TE modes can be fully solving for E_z and H_z respectively as all other field components can be derived from these two transverse fields [2], [3]. With this, (5-6) can be manipulated to solve for two independent 2-dimensional Helmholtz equations as

$$\nabla_t^2 E_z + k_c^2 E_z = 0 \quad \text{on } \Omega, \tag{7}$$

and

$$\nabla_t^2 H_z + k_c^2 H_z = 0 \quad \text{on } \Omega \tag{8}$$

where $\nabla_t^2 = \partial_x^2 + \partial_y^2$ the the trasverse Laplacian operator in cartesian coordinates, $k_c^2 = \omega^2\mu\epsilon - k_z^2$ is the cutoff wave number, k_z is the wavenumber in the direction of propagation, and Ω denotes all non-boundary locations within the simulation domain.

These relations hold for all locations excluding those on the PEC walls of the waveguide. This PEC wall condition manifests in the form of a Dirichlet boundary condition

$$E_z = 0 \quad \text{on } \partial\Omega \tag{9}$$

for the TM mode and Neumann boundary conditions

$$\partial_x H_z = 0,\ \partial_y H_z = 0 \quad \text{on } \partial\Omega \tag{10}$$

for the TE mode where $\partial\Omega$ denotes the PEC surface surrounding the waveguide.

2) Galerkin Weak Formulation: With the governing equations established, we can now proceed with the discretization of an arbitrarily shaped waveguide to solve for both the transverse electric and magnetic fields. Using FEM, we break these 2D waveguide slices into a finite set of finitely sized elements and approximate the solution of (7-8) over each element. Triangular elements are chosen as they can be meshed together to form the boundaries of arbitrarily curved shapes making them ideal for modeling geometries with no analytic solutions [3]. Linearly interpolating functions are used to approximate the solution of (7-8) at the nodes of each element. Linear interpolating functions are chosen for their overall simplicity and adequate accuracy for the determination of waveguide parameters [2], [3].

For an arbitrary triangular element, an generic scalar field ϕ can be Linearly interpolated over using

$$\phi^{(e)}(x,y) = a + bx + cy \tag{11}$$

where (e) refers to a specific element, a, b, c are scaling constants and x, y are the coordinates of the location within the node [3]. This interpolation scheme can now be applied to find the field value at an arbitrary node on the element as

$$\phi_l^{(e)} = a + bx_l + cy_l \tag{12}$$

where x, y are the coordinates of the node [3]. These nodal field expressions can now be combined to rewrite (11) in terms of the potentials calculated at each node as

$$\begin{aligned}\phi^{(e)}(x,y) = N_1^{(e)}(x,y)\phi_1^{(e)} \\ + N_2^{(e)}(x,y)\phi_2^{(e)} + N_3^{(e)}(x,y)\phi_3^{(e)}\end{aligned} \tag{13}$$

with an arbitrary interpolating function $N_l^{(e)}$ given by

$$N_l^{(e)}(x,y) = \frac{1}{2\Delta^{(e)}}\left(a_l^{(e)} + b_l^{(e)}x + c_l^{(e)}y\right) \tag{14}$$

where $\Delta^{(e)}$ is the area of element e and $a_l^{(e)}$, $b_l^{(e)}$, $c_l^{(e)}$ are given by the following as in [3]

$$\begin{aligned}a_1^e = x_2^e y_3^e - x_3^e y_2^e, b_1^e = y_2^e - y_3^e, c_1^e = x_3^e - y_2^e \\ a_2^e = x_3^e y_1^e - x_1^e y_3^e, b_2^e = y_3^e - y_1^e, c_2^e = x_1^e - y_3^e \\ a_3^e = x_1^e y_2^e - x_2^e y_1^e, b_3^e = y_1^e - y_2^e, c_3^e = x_2^e - y_1^e.\end{aligned} \tag{15}$$

With definitions (13-15) an arbitrary field with potential Dirichlet boundary conditions (noted by D) can be expressed as the superposition of all fields at each node as

$$\phi = \sum_{j=1}^{N} N_j\phi_j + \sum_{j=1}^{N} N_j^D\phi_j^D \tag{16}$$

With the discretization of a generic field outlined, The Galerkin weak forms of (7-8) will now be derived in parallel. We begin by multiplying (7-8) by a weighting function which is identical to that of an interpolating funcion for the Galerkin procedure such that $w_i = N_i$. The resulting weak forms are

$$\iint_\Omega N_i\left(\nabla_t^2 E_z + k_c^2 E_z\right) d\Omega = 0 \tag{17}$$

and

$$\iint_\Omega N_i\left(\nabla_t^2 H_z + k_c^2 H_z\right) d\Omega = 0. \tag{18}$$

In order for the linear weighting and basis functions N_i, N_j to work well, the laplacian term in 19-20 needs to be "spread-out". To accomplish this, integration by parts is exploited as follows

$$\begin{aligned}\iint_\Omega \left(\nabla_t N_i \cdot \nabla_t E_z - k_c^2 E_z N_i\right) d\Omega \\ = \left(N_i(\hat{n} \cdot \nabla_t E_z)\right)_{\partial\Omega}\end{aligned} \tag{19}$$

and

$$\iint_{\Omega} \left(\nabla_t N_i \cdot \nabla_t H_z - k_c^2 H_z N_i \right) d\Omega$$
$$= \left(N_i (\hat{n} \cdot \nabla_t H_z) \right)_{\partial\Omega} \quad (20)$$

With these forms in hand, we are now able to simplify the right hand sides of (19-20) using the boundary conditions found in (9-10). The right hand side of (19) disappears as E_z is explicitly set to zero on $\partial\Omega$ in the Dirichlet boundary condition (9). Likewise, the right hand side of (20) reduces to zero as the Neumann boundary condition in (10) sets $\nabla_t H_z = 0$. Despite the fact that both right hand sides reduce to zero, there is an important implementation detail that results in the final equations that arrises due to the Dirichlet term in (16). For simplicity, this term will be left out of the remaining equations however the impact of the Dirichlet term on (19) will be discussed in Section II-3.

Substituting in the generic field outlined in (16) with the exclusion of the Dirichlet term as previously mentioned results in the following general eigenvalue equations

$$[A]\{E_z\} = k_c^2 [B]\{E_z\} \quad (21)$$

and

$$[A]\{H_z\} = k_c^2 [B]\{H_z\} \quad (22)$$

to solve for the TM and TE modes respectively where $[A]$ and $[B]$ are sparse coefficient matrices. Individual coefficients in these matrices are calculated as

$$A_{ij} = \iint_{\Omega} \left(\nabla_t N_i \cdot \nabla_t N_j \right) d\Omega \quad (23)$$

and

$$B_{ij} = \iint_{\Omega} \left(N_i N_j \right) d\Omega. \quad (24)$$

3) Finite Element Matrix Assembly: With the Galerkin weak form of both Helmholtz equations derived, and the general eigenvalue problems established, we are now able to outline the assembly of the matrices $[A]$ and $[B]$. These matrices are constructed using the standard FEM matrix assembly process. Using this procedure, (23-24) are not explicitly calculated in one fell swoop for all (i, j). Rather, the contributions from each element are accumulated on local nodes (l, k) [3]. This allows for the assembly of the FEM matrices via a simple iteration over all elements without requiring all interactions between adjacent elements to be calculated ahead of time which would be costly. To facilitate this, a given meshing tool needs to provide the physical locations of all nodes as well as a connectivity list relating elements to their corresponding nodes.

Using the assembly process, and the analytical forms of the integrals of (23-24), the contributions of local nodes (l, k) on the global FEM matrices are as follows

$$A_{lk} = \frac{b_l^{(e)} b_k^{(e)} + c_l^{(e)} c_k^{(e)}}{4\Delta^{(e)}}, \quad (25)$$

and

$$B_{lk} = \frac{\Delta^{(e)}(1 + \delta_{lk})}{12} \quad (26)$$

where δ_{lk} is the Kronecker delta function which is the mathematical representation of the ternary statement: "δ_{lk} `= 1 ? (l==k) : 0;`".

With the procedure for assembling the FEM matrices outlined, it is now important to note the differences between $[A]$ and $[B]$ between the TM and TE modes. When solving the TM modes using 21, $[A]$ and $[B]$ contain nodes on $\partial\Omega$ as they are unknown. Thus $[A]$ and $[B]$ are both of size $n \times n$ where n is the number of nodes in the geometry. On the other hand, when solving for the TE mode using (22), nodes on $\partial\Omega$ are set to 0, as per the Dirichlet boundary condition, thus do not explicitly contribute to $[A]$ and $[B]$. As such, these matrices are both of size $(n - b) \times (n - b)$ where b is the number of nodes on the boundary.

III. Numerical Results

With the mathematical model now fully established we now proceed to discus the implementation of this model in Section III-A. From here Sections III-B verifies the model against exact dispersion relations for multiple modes in rectangular waveguides. Section III-C performs an analysis of Dispersion characteristics in circular waveguides and addresses the advantages of using FEA for this task. Finally, Section III-D compares the dispersion characteristics of the rectangular and ridged rectangular waveguides for multiple modes and discusses practical applications of ridged waveguides.

A. Implementation

All meshes used in the following sections were generated using Coreform Cubit [4] with a tutorial provided by [2]. For the rectangular waveguide found in III-B, a WR-90, X-band waveguide with $a = 0.02286$m and $b = 0.01016$m was used [5]. For the circular waveguide used in III-C, a similarly sized circular waveguide of radius $r = 0.01$m was used. In order to compare the non-ridged to the ridged waveguide the same WR-90, X-band waveguide was used in Section III-D as in Section III-B however with two 0.0025×0.0025m notches cut out along the long edge. Example meshes of the later two geometries can be found in Figures 1-2. These meshes were generated using Coreform Cubit's `TriAdvance` algorithm all containing ≈ 2000 elements which is appropriate for the applications studied here. Coreform Cubit's `nodeset` feature was used to create a set of all nodes on the boundaries of these geometries. This allows for $O(1)$ lookups of elements on the boundary which was utilized heavily when performing TE mode analysis. These meshes were saved into the ANSYS `.inp` ASCII format which was chosen as it is human readable which was invaluable during the development of this code.

The mathematical model outlined in Section II was implemented in Python for its general flexibility and existing numerical packages such as NumPy and SciPy which were used to solve the general eigenvalue problems established in (22-21). In addition to these packages, the MeshIO package

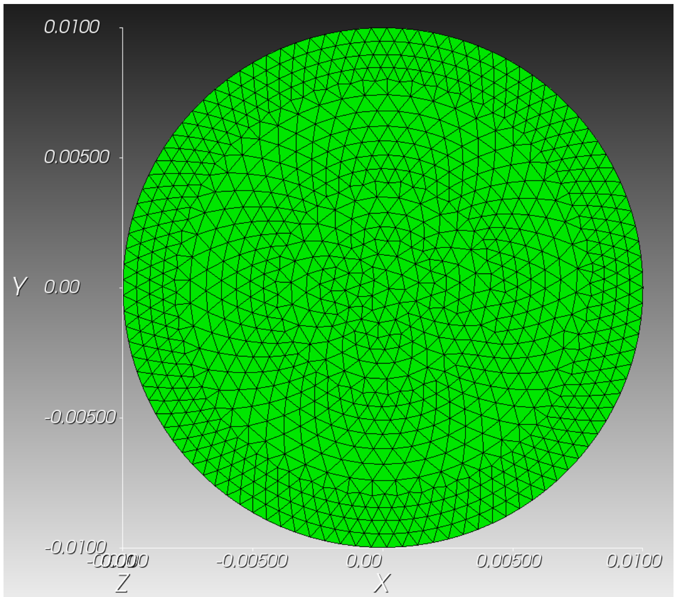

Fig. 1: Circular Waveguide Mesh used in Section III-C

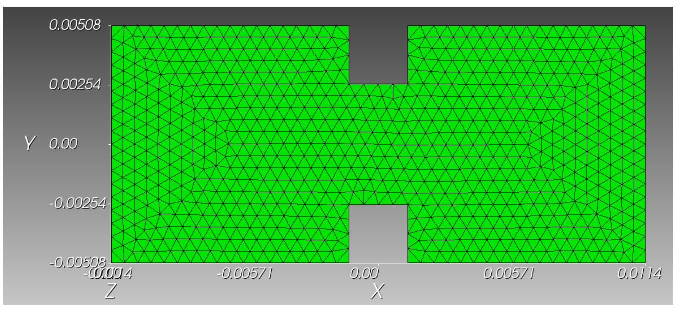

Fig. 2: Ridged Rectangular Waveguide Mesh used in Section III-D

was used as it has a built in reader for `.inp` files allowing mesh data to be read in with ease. From this, all generated data was directly plotted using Matplotlib thereby eliminating the need to save any generated data to disk.

B. Verification and Validation

Prior to performing any kind of 'novel' analysis, the implemented model must first be benchmarked against analytic results. For this reason, we will first consider the case of a WR-90, X-band waveguide WR-90, X-band waveguide with $a = 0.02286$m and $b = 0.01016$m [5].

In this and all following sections the spatial distributions of TE modes will be plotted. Only one mode will be plotted per section as these are merely visual aids in comparison to the dispersion charts which will contain data from the first 3 TE and TM modes. The choice of the given TE mode is entirely arbitrary and was chosen for its post processing simplicity and to ensure adequate comparisons exist in the literature [1]. The TE_{11}, H_z field distribution can be found in Fig. 3. As seen in Fig. 3 the TE_{11}, H_z field profile matches that of the TE_{11} found in the literature thus confirming its accuracy in recreating spatial field profiles.

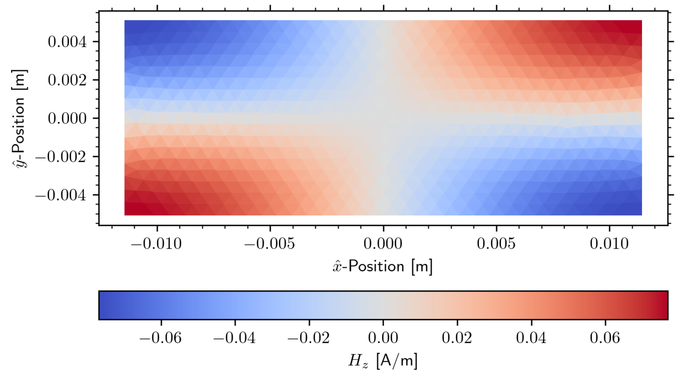

Fig. 3: TE_{11}, H_z Field Distribution in a Rectangular WR-90, X-band Waveguide

Next, a dispersion plot of the first three TE and TM modes in this waveguide is constructed. To benchmark to theory, the following analytic cutoff wave number is used

$$k_c = \sqrt{\left(\frac{m\pi}{a}\right)^2 + \left(\frac{n\pi}{b}\right)^2} \tag{27}$$

where m and n are the corresponding mode propagation numbers. From this, the first three, unique and nonzero simulated cutoff wave numbers from both the TE and TM modes were used to create the dispersion plot in Fig. 4.

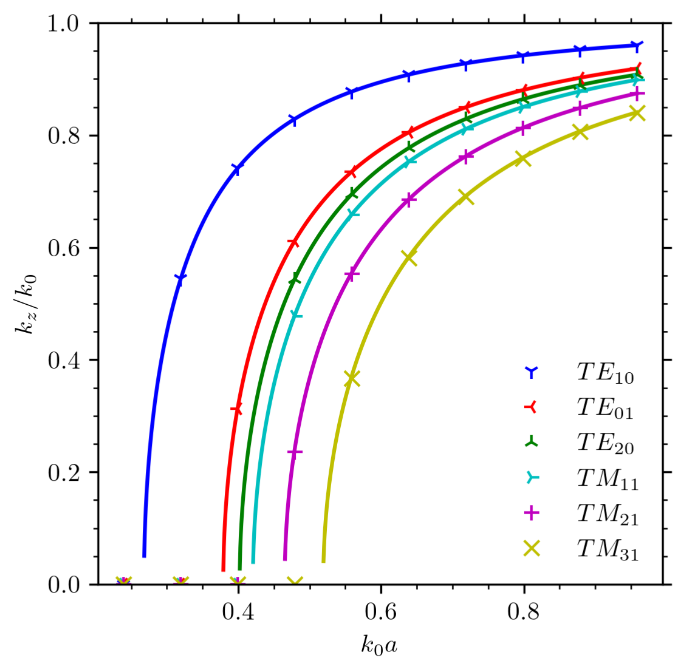

Fig. 4: TE_{11}, H_z Field Distribution in a Rectangular WR-90, X-band Waveguide with Solid Lines as the Theoretical Dispersion Relation and Corresponding Markers as Simulated Dispersion Relation

As seen in Fig. 4, the dispersion relations predicted by the implemented model match that predicted by theory excellently. With this, we move on to assess more sophisticated waveguides knowing that the underlying mathematical model is sound.

C. Circular Waveguides

With the model successfully validated against the analytic results of a rectangular waveguide, we now move to assess a circular waveguide of radius $r = 0.01$m.

D. Comparison of Ridged and Non-Ridged Waveguides

IV. Conclusion

A 3-dimensional finite difference time domain was developed from Maxwell's Equations for a rectangular waveguide and cavity resonator. The model was validated against analytic results for narrow and wide band signals thereby verifying the model's calculated fields. From this, several dielectric materials were compared for use in X-Band cavity resonators at 10GHz. These compared results were then explained using theoretical unloaded quality factors vurther verifying the accuracy of the model.

While relatively performant, there are many optimizations that could be made to the underlying implementation. Most notably tiled approaches could be taken to improve program cache locality to alleviate the memory bound nature of the loops in this implementation. Tiled approaches would also aid in exploiting the embarrassingly parallel structure Yee's FDTD algorithm gives rise to. Further improvements could also be made to the implementation to allowing for more complex geometries to be represented which may be useful for placing devices inside waveguides or using the waveguide as a source for another device. Finally, the user experience of this implementation should be improved as it is remarkably easy to save in tens to hundreds of gigabytes of data inadvertently shifting the bottleneck away from memory to disk performance.

References

[1] D. M. Pozar, *Microwave Engineering*. John Wiley & Sons, 2011.

[2] T. E. Roth, *ECE 61800 Lecture Notes*. Purdue University, 2024.

[3] J.-M. Jin, *Theory and Computation of Electromagnetic Fields*. John Wiley & Sons, 2011.

[4] Coreform LLC, "Coreform cubit," https://coreform.com/products/coreform-cubit/, 2024, [Online; accessed 26-March-2024].

[5] Everything RF contributors, "Rectangular waveguide sizes," https://www.everythingrf.com/tech-resources/waveguides-sizes, 2021, [Online; accessed 28-Feburary-2024].